ELSEVIER

Finite element formulation for active functionally graded thin-walled structures

Hanen Jrad *, Hanen Mallek, Mondher Wali, Fakhreddine Dammak

Engineering Production Mechanics and Materials Unit (UGPM2), National Engineering School of Sfax, B.P. W3038, Sfax, University of Sfax, Tunisia

ARTICLE INFO

ABSTRACT

For the analysis and design process of smart structures with integrated piezoelectric patches, the finite element method provides an effective simulation approach. In this paper, an attempt on modeling and simulation of the behavior of hybrid active structures is carried out using developed Kirchhoff-type-four-node shell element.

The finite element results are compared with reference solutions taking into account the electromechanical responses of smart structures with various geometries, and the results show very high agreement. The main aspect of the application of the proposed element is to predict the behavior of FGM shells containing piezoelectric layers. A set of numerical analyses is performed in order to highlight the applicability and effectiveness of the present finite element model, notably for smart FGM structures. A comprehensive parametric study is conducted to show the influence of material composition, the placement and the thickness of the piezoelectric layers on the deformation of the laminated structure.

© 2018 Académie des sciences. Published by Elsevier Masson SAS. All rights reserved.

1. Introduction

The requirement of structural strength in many engineering fields demands materials that can maintain structural integrity. Although the great developments made in the design of structures using classical materials, such structures are considered as passive systems. Indeed, they are dimensioned in order to sustain the most critical loads that occur during the lifetime of the structure; however, there is no possibility of active improvement of the behavior of the structure during loading, especially critical and unexpected loading, which has a significant influence on the robustness of the system. In order to overcome those drawbacks of passive systems, active or smart structure are introduced.

Smart structures have attracted intensive research interests because of their potential benefits in a wide range of applications, such as shape control, vibration suppression, noise attenuation, and damage detection [1,2]. Several materials that exhibit physical coupling effects can be employed in active structures as integrated sensors/actuators, e.g., piezoelectrics, shape memory alloys (SMAs), electrostrictive materials, electro-rheological fluids or polymer gels, for instance. The most frequently used active materials are the piezoelectric ones. The coupled mechanical and electrical properties of piezoelectric materials make them well suited for use as sensors and actuators in smart structures, named also intelligent structures. These structures offer great potential for use in advanced aerospace as well as hydrospace, nuclear and automotive structural applications due to their excellent electromechanical properties, easy fabrication, design flexibility, and efficiency to convert

---

electrical energy into mechanical energy [3–8]. In fact, their intrinsic electromechanical coupling effect produces mechanical deformations under the application of electrical loads (i.e. the direct effect) and electrical fields under the application of mechanical loads (i.e. the converse effect). Hence, it is important to develop efficient computational tools to predict the electromechanical coupling behavior of these advanced structures.

Recently, functionally graded materials (FGMs) have found extensive applications in a variety of industries such as aeronautical production industry, mechanical engineering, and nuclear engineering due to their distinctive material properties that vary continuously and smoothly through certain dimensions. Compared with common composites, FGMs have several advantages, namely, assuring continuous transition of stress distributions, reducing or removing of stress concentration, and consolidating bonding strength along the interface of two dissimilar materials [9–11]. On the other hand, piezoelectric applications as distributed sensors and actuators use thin piezoelectric patches embedded or bonded to a surface made from composite materials. Within this framework, the aim of this research is to provide an accurate description of the electromechanical coupling behavior of piezolaminated structures composed of piezoelectric patches bonded to FGM surfaces.

Furthermore, due to the increasing use of composite structures in advanced industries, it is crucial to apply an appropriate theory in conjunction with a consistent and powerful numerical approach such as the finite element method. Shell elements are the key structures widely used in various mechanical structures, civil engineering, aerospace and naval, due to their excellent performance. Over the years, modeling and analysis of the behavior of shell structures have received considerable attention from research communities: see [12–27], to cite a few works. It is found that kinematics of typical shell structures can be described using three theories: (i) Kirchhoff–Love theory; (ii) First-order Shear Deformation Theory (FSDT); (iii) High-order Shear Deformation Theories (HSDT). Although Kirchhoff theory neglects the effect of shear deformations, it has proved its efficiency in describing the behavior for thin shells by its simple implementation in the most finite element codes and low computational cost. In order to deal with the restriction of Kirchhoff's model, Reissner and Mindlin proposed First order Shear Deformation Theory (FSDT) to take into account the shear deformation effect. Nevertheless, the Reissner and Mindlin's approach seems to be insufficient to examine thick shell structures; besides, it is necessary to introduce shear correction coefficients that can be restrictive for such applications. Indeed, shear correction coefficients can be simply acquired for linear isotropic material (5/6), but their determination is more complex for composites, especially laminated structures. High-order Shear Deformation Theories were proposed to overcome the shear coefficients limitations. Despite these theories provide a refined approximation of the displacements and deformations of the structure, the number of used kinematic variables is mainly high, which leads to difficult numerical resolution, particularly for complex geometries.

Moreover, several investigations have been carried out to describe the mechanical behavior of composite structures and, recently, of FGM materials based on solid-shell finite elements; the interested reader is referred to [28–33], among other publications. The formulation of these 3D elements has been developed based on several combinations of Enhanced Assumed Strain (EAS) and Assumed Natural Strain (ANS) methods in order to prevent most locking phenomena, which improves their efficiency in the prediction of various mechanical aspects of shell structures. Although commercial FEA software packages like ANSYS and ABAQUS have coupled field analysis efficiency which can deal with the electro-thermomechanical behavior of piezoelectric materials, only 3D piezoelectric solid finite elements can be treated, while most piezoelectric applications as dispersed sensors and actuators use thin piezoelectric patches embedded or bonded to a surface made of composite materials. Hence, the application of these elements for the analysis of thin-walled active structures involves significant numerical executions and higher computation cost. Consequently, several researchers in this field have dedicated their work to the development of more adequate 2D finite element methods that provide good precision with less numerical operations [34–41]. The choice of the appropriate kinematic model for accurate analysis of advanced composite structure is still one of the most challenging problems in finite element simulations. Taking into account the rapid development of computer technologies and numerical methods in engineering and in order to assure a compromise between accuracy and low computational effort, the Kirchhoff model seems to be a suitable choice to examine the electromechanical coupling behavior of thin-walled active structures with laminate architectures featuring FGM composite as a passive material and utilizing piezoelectric patches as both sensor and actuator components.

2. Piezoelectric Kirchhoff shell formulation

In this section, the geometry and kinematics of the linear discrete Kirchhoff shell model are briefly described. The reference surface of the shell is assumed to be smooth, continuous and differentiable. The initial and the deformed configurations are denoted by C_0 and C_t, respectively.

Variables associated with initial configuration C_0 are denoted by uppercase letters, whereas those related to current configuration C_t are symbolized using lowercase letters. To distinguish vectors from other variables, they are expressed using bold letters.

2.1. Piezoelectric Kirchhoff shell kinematic assumptions

The position vector of any material point (q), which is located at a distance z along the shell director $\boldsymbol{D}$, is defined in terms of curvilinear coordinates $\boldsymbol{\xi} = (\xi^1, \xi^2, \xi^3 = z)$ as follows:

$$\boldsymbol{X}_q(\xi^1, \xi^2, z) = \boldsymbol{X}_p(\xi^1, \xi^2) + z\boldsymbol{D}(\xi^1, \xi^2), \quad z \in [-h/2, h/2] \tag{1}$$
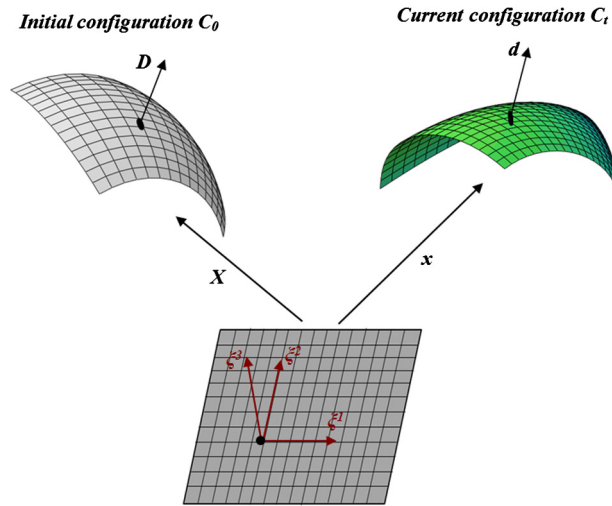
Fig. 1. Parameterizations of the shell material points: the initial and current configuration of the shell structure.

in which h is the thickness, p represents the material point located on the reference surface of the shell, and $\boldsymbol{D}$ is the initial shell director, as illustrated in Fig. 1.

The base vectors are represented in the initial state C_0 by:

$$\boldsymbol{G}_\alpha = \boldsymbol{A}_\alpha + z\boldsymbol{D}_{,\alpha}; \qquad \boldsymbol{G}_3 = \boldsymbol{D}, \quad \alpha = 1, 2 \tag{2}$$

The surface element $\mathrm{d}A$ in the initial state is given by:

$$\mathrm{d}A = \sqrt{A}\,\mathrm{d}A_\xi, \qquad \sqrt{A} = \|\boldsymbol{A}_1 \wedge \boldsymbol{A}_2\|, \qquad \mathrm{d}A_\xi = \mathrm{d}\xi^1 \mathrm{d}\xi^2 \tag{3}$$

The covariant reference metric tensor $\boldsymbol{G}$ at a material point $\boldsymbol{\xi}$ is defined by:

$$\boldsymbol{G} = [\boldsymbol{G}_i.\boldsymbol{G}_j], \quad i, j = 1, 2, 3 \tag{4}$$

The volume element $\mathrm{d}V$ in the initial state is given by:

$$\mathrm{d}V = \sqrt{G}\,\mathrm{d}\xi^1\,\mathrm{d}\xi^2\,\mathrm{d}z, \quad \sqrt{G} = [\boldsymbol{G}_1 \quad \boldsymbol{G}_2 \quad \boldsymbol{G}_3] = \sqrt{|G_{ij}|} \tag{5}$$

The metric tensor in the deformed configuration C_t can be divided into two parts: the first one takes into account the in-plane components, while the second one involves the out-of-plane components. Hence, it is expressed as:

$$g_{ij} = \boldsymbol{g}_i.\boldsymbol{g}_j, \qquad \begin{cases} g_{\alpha\beta} = a_{\alpha\beta} + zb_{\alpha\beta} \\ g_{\alpha3} = c_\alpha \end{cases} \quad \alpha, \beta = 1, 2 \tag{6}$$

where $a_{\alpha\beta}$, $b_{\alpha\beta}$ and c_α represent kinematic variables, which are expressed as:

$$\begin{cases} a_{\alpha\beta} = \boldsymbol{a}_\alpha \cdot \boldsymbol{a}_\beta \\ c_\alpha = \boldsymbol{a}_\alpha \cdot \boldsymbol{d} \\ b_{\alpha\beta} = \boldsymbol{a}_\alpha \cdot \boldsymbol{d}_{,\beta} + \boldsymbol{a}_\beta \cdot \boldsymbol{d}_{,\alpha} \end{cases} \tag{7}$$

The Lagrangian strain $\boldsymbol{\varepsilon}$ can be formulated as a function of membrane, bending, and transverse shear strains using the following expression:

$$\boldsymbol{\varepsilon} = \frac{1}{2}(\boldsymbol{g} - \boldsymbol{G}), \qquad \varepsilon_{ij} = \frac{1}{2}(g_{ij} - G_{ij}), \qquad \begin{cases} \varepsilon_{\alpha\beta} = e_{\alpha\beta} + z\chi_{\alpha\beta} \\ 2\varepsilon_{\alpha3} = \gamma_\alpha \end{cases} \tag{8}$$

where $e_{\alpha\beta}$, $\chi_{\alpha\beta}$ and γ_α denote respectively the membrane, bending, and transverse shear strains. In matrix notation, these components are given by:

$$\boldsymbol{e} = \begin{Bmatrix} e_{11} \\ e_{22} \\ 2e_{12} \end{Bmatrix}, \qquad \boldsymbol{\chi} = \begin{Bmatrix} \chi_{11} \\ \chi_{22} \\ 2\chi_{12} \end{Bmatrix}, \qquad \boldsymbol{\gamma} = \begin{Bmatrix} \gamma_1 \\ \gamma_2 \end{Bmatrix} \tag{9}$$

Moreover, the virtual components are computed in the initial configuration C_0 as:

$$\delta e_{\alpha\beta} = 1/2(\boldsymbol{A}_\alpha \cdot \delta\boldsymbol{x}_{,\beta} + \boldsymbol{A}_\beta \cdot \delta\boldsymbol{x}_{,\alpha}); \qquad \delta\gamma = \boldsymbol{A}_\alpha \cdot \delta\boldsymbol{d} + \delta\boldsymbol{x}_{,\alpha} \cdot \boldsymbol{d}$$
$$\delta\chi_{\alpha\beta} = 1/2(\boldsymbol{A}_\alpha \cdot \delta\boldsymbol{d}_{,\beta} + \boldsymbol{A}_\beta \cdot \delta\boldsymbol{d}_{,\alpha} + \delta\boldsymbol{x}_{,\alpha} \cdot \boldsymbol{d}_{,\beta} + \delta\boldsymbol{x}_{,\beta} \cdot \boldsymbol{d}_{,\alpha}); \quad \boldsymbol{d} = \boldsymbol{D}; \alpha, \beta = 1, 2 \tag{10}$$

It should be emphasized that, according to the Kirchhoff approach, the shear contribution of strain disappears in discrete form over the element boundary side and becomes indeed zero [42].

The electrical field $\boldsymbol{E}$ is evaluated based on the gradient of the electric potential φ. Its expression is given by:

$$\boldsymbol{E} = -\varphi_{,\alpha}, \quad \alpha = 1, 2, 3 \tag{11}$$

The in-plane electric field components E_1 and E_2 are neglected and only the transverse electric field E_3 is considered. The electric field of an element in terms of the electrical potential is expressed as:

$$E_1 = 0; \qquad E_2 = 0; \qquad E_3 = -\frac{\partial\varphi}{\partial z} \tag{12}$$

2.2. Weak form

The Lagrangian formulation uses scalars, and so coordinate transformations tend to be much easier. By using the total Lagrangian formulation, the weak form of the equilibrium equations can take the following form:

$$G(\boldsymbol{\Phi}, \delta\boldsymbol{\Phi}) = \int_V (\sigma_{ij} \cdot \delta\varepsilon_{ij} + q_i\delta E_i)\,\mathrm{d}V - G_{\text{ext}}(\delta\boldsymbol{\Phi}) = 0 \tag{13}$$

where $\delta\boldsymbol{\Phi} = (\delta\boldsymbol{x}, \delta\boldsymbol{d}, \delta\varphi)$ is an arbitrary variation, $\delta\varepsilon_{ij}$ are the components of the strain tensor, σ_{ij} are the components of the stress tensor, q_i is the electric displacement, δE_i is the virtual electric vector, and G_{ext} is the external virtual work.

Using Eqs. (8) and (9), the weak form becomes:

$$G = \int_A (\boldsymbol{N} \cdot \delta\boldsymbol{e} + \boldsymbol{M} \cdot \delta\boldsymbol{\chi} + \bar{\boldsymbol{q}}\delta\boldsymbol{E})\,\mathrm{d}A - G_{\text{ext}} = 0 \tag{14}$$

where $\delta\boldsymbol{e}$ and $\delta\boldsymbol{\chi}$ are the variations of the shell strains, $\boldsymbol{N}$ and $\boldsymbol{M}$ are the membrane and bending stress resultants, and $\bar{\boldsymbol{q}}$ is the electric displacement, which can be expressed in matrix form as:

$$\boldsymbol{N} = \left\{ \begin{array}{c} N^{11} \\ N^{22} \\ N^{12} \end{array} \right\}, \qquad \boldsymbol{M} = \left\{ \begin{array}{c} M^{11} \\ M^{22} \\ M^{12} \end{array} \right\}, \qquad \bar{\boldsymbol{q}} = \left\{ \begin{array}{c} q^{11} \\ q^{22} \\ q^{33} \end{array} \right\} \tag{15}$$

Their components are defined as follows:

$$N^{\alpha\beta} = \int_{-h/2}^{h/2} \sigma_{\alpha\beta}\sqrt{G/A}\,\mathrm{d}z, \qquad M^{\alpha\beta} = \int_{-h/2}^{h/2} z\sigma_{\alpha\beta}\sqrt{G/A}\,\mathrm{d}z, \qquad \bar{q}^{\alpha\beta} = \int_{-h/2}^{h/2} q^{\alpha\beta}\sqrt{G/A}\,\mathrm{d}z \tag{16}$$

The expressions of the generalized resultant of stress $\boldsymbol{R}$ and strain $\boldsymbol{\Sigma}$ vectors are given by:

$$\boldsymbol{R} = \left\{ \begin{array}{c} \boldsymbol{N} \\ \boldsymbol{M} \\ \bar{\boldsymbol{q}} \end{array} \right\}_{9\times1}, \qquad \boldsymbol{\Sigma} = \left\{ \begin{array}{c} \boldsymbol{e} \\ \boldsymbol{\chi} \\ \boldsymbol{E}_m \end{array} \right\}_{9\times1} \tag{17}$$

Hence, the weak form of the equilibrium equation can be rewritten as

$$G(\boldsymbol{\Phi}, \delta\boldsymbol{\Phi}) = \int_A \delta\boldsymbol{\Sigma}^\mathsf{T} \cdot \boldsymbol{R}\,\mathrm{d}A - G_{\text{ext}}(\boldsymbol{\Phi}, \delta\boldsymbol{\Phi}) = 0 \tag{18}$$

2.3. Constitutive equations of the piezoelectric Kirchhoff shell

Both direct and converse piezoelectric effects are expressed using the piezoelectric constitutive equations coupling the elastic and electric fields and formulated as follows:

$$\begin{cases} \boldsymbol{\sigma} = \boldsymbol{C}\boldsymbol{\varepsilon} - \boldsymbol{p}^\mathsf{T}\boldsymbol{E} \\ \boldsymbol{q} = \boldsymbol{p}\boldsymbol{\varepsilon} + \boldsymbol{g}\boldsymbol{E} \end{cases} \tag{19}$$

where $\boldsymbol{q}$ is the electric displacement vector, $\boldsymbol{p}$ is the piezoelectric coupling matrix, and $\boldsymbol{g}$ is the dielectric permittivity matrix. $\boldsymbol{E}$ denotes the electric field vector, $\boldsymbol{\sigma}$ is the stress vector, $\boldsymbol{\varepsilon}$ represents the strain tensor, and $\boldsymbol{C}$ is the elastic matrix for a constant electric field.

In the case of an elastic isotropic constitutive model, the stress resultant $\mathbf{R}$ is related to the strain field:

$$\boldsymbol{R} = \boldsymbol{H}_T \boldsymbol{\Sigma} \tag{20}$$

with $\boldsymbol{H}_T$ is the linear coupling elastic and electric matrix expressed as:

$$\boldsymbol{H}_T = \begin{bmatrix} \boldsymbol{H}_{11} & \boldsymbol{H}_{12} & \boldsymbol{H}_{13} \\ & \boldsymbol{H}_{22} & \boldsymbol{H}_{23} \\ Sym & & \boldsymbol{H}_{33} \end{bmatrix}; \quad \begin{cases} (\boldsymbol{H}_{11}, \boldsymbol{H}_{12}, \boldsymbol{H}_{22}) = \int_{-h/2}^{h/2}(1, z, z^2)\boldsymbol{C}\,\mathrm{d}z \\ (\boldsymbol{H}_{13}, \boldsymbol{H}_{23}) = \int_{-h/2}^{h/2}(1, z)\boldsymbol{p}^\mathsf{T}\,\mathrm{d}z \\ \boldsymbol{H}_{33} = \int_{-h/2}^{h/2} \boldsymbol{g}\,\mathrm{d}z \end{cases} \tag{21}$$

where $\boldsymbol{C}$ is the in-plane linear elastic sub-matrix, which can be written as:

$$\boldsymbol{C} = \frac{Y(z)}{1 - \nu^2(z)} \begin{bmatrix} 1 & \nu(z) & 0 \\ \nu(z) & 1 & 0 \\ 0 & 0 & (1-\nu(z))/2 \end{bmatrix} \tag{22}$$

in which $Y(z)$ is the Young modulus and $\nu(z)$ is Poisson's ratio.

$\boldsymbol{p}^\mathsf{T}$ represents the in-plane dielectric permittivity sub-matrices that can be expressed as:

$$\boldsymbol{p}^\mathsf{T} = \begin{bmatrix} 0 & 0 & e_{31} \\ 0 & 0 & e_{32} \\ 0 & 0 & 0 \end{bmatrix} \tag{23}$$

3. Finite element formulation

The finite element implementation of the present theoretical formulation based on a four-node linear Kirchhoff shell element is presented in this section, in order to predict static electromechanical responses of a piezolaminated structure composed of piezoelectric patches bonded to a composite surface. Thus, the development of an isoparametric finite element, which is of displacement–rotation–electric potential type, can be carried out. The proposed element has six degrees of freedom: $u, v, w, \theta_x, \theta_y, \varphi$.

The interpolation of the displacement vector ($\boldsymbol{U} = \boldsymbol{x} - \boldsymbol{X}$) and of the shell vector $\boldsymbol{d}$ can be written as:

$$\boldsymbol{U} = \sum_{I=1}^{4} N^I \boldsymbol{U}_I, \qquad \boldsymbol{d} = \sum_{I=1}^{4} N^I \boldsymbol{d}_I + \sum_{K=5}^{8} P^K \alpha_K \boldsymbol{t}_K \tag{24}$$

with $\boldsymbol{U}_I \in R^3$, $\boldsymbol{d}_I$ is the shell vector at the nodal points, (I) represents a node of the element, and N^I denotes the standard bilinear isoparametric shape functions.

(K) represents the mid-point of the element boundaries and α_K are variables associated with $\boldsymbol{d}$ on the element boundaries. The vector $\boldsymbol{t}_K$ is the unit vector and its direction is defined by the position of the nodes couple (I, J), as depicted in Fig. 2,

$$\boldsymbol{t}_K = (\boldsymbol{x}_J - \boldsymbol{x}_I)/L_K, \quad L_K = \|\boldsymbol{x}_J - \boldsymbol{x}_I\| \tag{25}$$

where L_K is the I–J side length.

The expressions of the shape functions for the quadrilateral elements N^I and P^K are given respectively in Table 1.

The electric potential φ can be interpolated from the nodal electric potential vectors φ_n:

$$\varphi = \sum_{I=1}^{4} N^I \varphi_I \tag{26}$$

The relation between the derivation of N^I in the local Cartesian and the local elementary systems can be written as:

$$\begin{Bmatrix} \bar{N}^I_{,1} \\ \bar{N}^I_{,2} \end{Bmatrix} = [\boldsymbol{J}]^{-1} \begin{Bmatrix} N^I_{,1} \\ N^I_{,2} \end{Bmatrix} \tag{27}$$

where $\boldsymbol{J}$ is the Jacobian transformation from the local Cartesian base $\{\boldsymbol{n}_1^0, \boldsymbol{n}_2^0, \boldsymbol{n}^0\}$ to the covariant base $\{\boldsymbol{A}_1, \boldsymbol{A}_2, \boldsymbol{A}_3\}$ as shown in Fig. 3. It can be defined as:
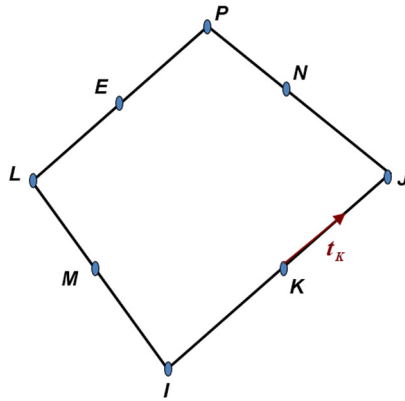
Fig. 2. Position of the nodes couple (I, J).

Table 1
Shape functions N^I and P^K for a quadrilateral element.

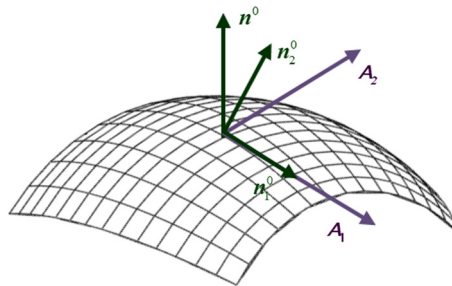|	
$N^1 = \frac{1}{4}(1-\xi)(1-\eta)$	$P^5 = \frac{1}{2}(1-\xi^2)(1-\eta)$
$N^2 = \frac{1}{4}(1+\xi)(1-\eta)$	$P^6 = \frac{1}{2}(1+\xi)(1-\eta^2)$
$N^3 = \frac{1}{4}(1+\xi)(1+\eta)$	$P^7 = \frac{1}{2}(1-\xi^2)(1+\eta)$
$N^4 = \frac{1}{4}(1-\xi)(1+\eta)$	$P^8 = \frac{1}{2}(1-\xi)(1-\eta^2)$

Fig. 3. Single-layer shell with system coordinates.

$$J = \begin{bmatrix} \boldsymbol{n}_1^0 \cdot \boldsymbol{A}_1 & \boldsymbol{n}_2^0 \cdot \boldsymbol{A}_1 \\ \boldsymbol{n}_1^0 \cdot \boldsymbol{A}_2 & \boldsymbol{n}_2^0 \cdot \boldsymbol{A}_2 \end{bmatrix} \tag{28}$$

The normal field $\boldsymbol{n}^0$ to the mid-surface, in the initial state C_0, can be evaluated as:

$$\boldsymbol{n}^0 = \frac{\boldsymbol{A}_1 \wedge \boldsymbol{A}_2}{\|\boldsymbol{A}_1 \wedge \boldsymbol{A}_2\|} \tag{29}$$

3.1. Approximation of the membrane strain field

The discretization of the membrane part of the strain field is given by:

$$\delta \boldsymbol{e} = \boldsymbol{B}_\mathrm{m} \cdot \delta \boldsymbol{\Phi}_n \tag{30}$$

where $\boldsymbol{B}_\mathrm{m}$ represents the membrane strain–displacement matrix. Their expressions are given at nodal level I as follows:

$$\boldsymbol{B}_\mathrm{m}^I = [\, \boldsymbol{B}_\mathrm{mm}^I \quad \boldsymbol{0} \quad \boldsymbol{0} \,], \qquad \boldsymbol{B}_\mathrm{mm}^I = \begin{bmatrix} \boldsymbol{n}_1^{0\top} \bar{N}_{,1}^I \\ \boldsymbol{n}_2^{0\top} \bar{N}_{,2}^I \\ \boldsymbol{n}_1^{0\top} \bar{N}_{,2}^I + \boldsymbol{n}_2^{0\top} \bar{N}_{,1}^I \end{bmatrix}, \quad I = 1, \dots, 4 \tag{31}$$

3.2. Approximation of bending strain field

The discretization of bending strain is expressed as

$$\delta \boldsymbol{\chi} = \boldsymbol{B}_{\mathrm{b}} \cdot \delta \boldsymbol{\Phi}_n \tag{32}$$

where $\boldsymbol{B}_{\mathrm{b}}$ is the discrete bending strain–displacement matrix. It can be defined by:

$$\boldsymbol{B}_{\mathrm{b}}^I = [\, \boldsymbol{B}_{\mathrm{bm}}^I \quad \boldsymbol{B}_{\mathrm{bb}}^I \quad \boldsymbol{0} \,] \tag{33}$$

$$\boldsymbol{B}_{\mathrm{bm}}^I = \begin{bmatrix} \boldsymbol{d}_{2,1}^{\mathsf{T}} \bar{N}_{,1}^I + \boldsymbol{n}_1^{0\mathsf{T}} \boldsymbol{M}_{d,1}^I \\ \boldsymbol{d}_{2,2}^{\mathsf{T}} \bar{N}_{,2}^I + \boldsymbol{n}_2^{0\mathsf{T}} \boldsymbol{M}_{d,2}^I \\ \boldsymbol{d}_{2,1}^{\mathsf{T}} \bar{N}_{,2}^I + \boldsymbol{n}_1^{0\mathsf{T}} \boldsymbol{M}_{d,2}^I + \boldsymbol{d}_{2,2}^{\mathsf{T}} \bar{N}_{,1}^I + \boldsymbol{n}_2^{0\mathsf{T}} \boldsymbol{M}_{d,1}^I \end{bmatrix}, \qquad \boldsymbol{B}_{\mathrm{bb}}^I = \begin{bmatrix} \boldsymbol{n}_1^{0\mathsf{T}} \cdot \boldsymbol{M}_{r,1}^I \\ \boldsymbol{n}_2^{0\mathsf{T}} \cdot \boldsymbol{M}_{r,2}^I \\ \boldsymbol{n}_1^{0\mathsf{T}} \cdot \boldsymbol{M}_{r,2}^I + \boldsymbol{n}_2^{0\mathsf{T}} \cdot \boldsymbol{M}_{r,1}^I \end{bmatrix} \tag{34}$$

The matrices $\boldsymbol{M}_d^I$ and $\boldsymbol{M}_r^I$ are expressed as:

$$\boldsymbol{M}_d^I = P_K \boldsymbol{td}_K^I + P_M \boldsymbol{td}_M^I, \quad \boldsymbol{td}_K^I = \frac{3}{2L_K} \boldsymbol{t}_K \otimes \boldsymbol{d}_K \tag{35}$$

$$\boldsymbol{M}_r^I = N^I \boldsymbol{I} + P_K \boldsymbol{tt}_K^I + P_M \boldsymbol{tt}_M^I, \quad \boldsymbol{tt}_K^I = \frac{3}{4} \boldsymbol{t}_K \otimes \boldsymbol{t}_K \tag{36}$$

3.3. Approximation of the electric field

The electric field is interpolated as follows:

$$\delta \boldsymbol{E}_{\mathrm{m}} = \boldsymbol{B}_{\mathrm{e}} \cdot \delta \boldsymbol{\Phi}_n \tag{37}$$

where $\boldsymbol{B}_{\mathrm{e}}$ represents the discrete electric field–displacement vector and $\boldsymbol{E}_{\mathrm{m}}$ denotes the opposite of the electrical field $\boldsymbol{E}$.

$$\boldsymbol{B}_{\mathrm{e}} = [\, \boldsymbol{0} \quad \boldsymbol{0} \quad \boldsymbol{B}_{\mathrm{e}}^I \,]; \quad \boldsymbol{B}_{\mathrm{e}}^I = \begin{Bmatrix} 0 \\ 0 \\ \frac{N^I}{t} \end{Bmatrix} \tag{38}$$

Finally, the generalized strain $\delta \boldsymbol{\Sigma}$ can be approximated as follows:

$$\delta \boldsymbol{\Sigma} = \begin{Bmatrix} \delta \boldsymbol{e} \\ \delta \boldsymbol{\chi} \\ \delta \boldsymbol{E}_{\mathrm{m}} \end{Bmatrix} = \boldsymbol{B} \cdot \delta \boldsymbol{\Phi}_n, \qquad \boldsymbol{B} = \begin{bmatrix} \boldsymbol{B}_{\mathrm{m}} \\ \boldsymbol{B}_1 \\ \boldsymbol{B}_2 \\ \boldsymbol{B}_s \\ \boldsymbol{B}_{\mathrm{e}} \end{bmatrix} \tag{39}$$

Using Eqs. (20) and (39), the internal virtual work becomes:

$$G_{\mathrm{int}} = \int_A \delta \boldsymbol{\Sigma}^{\mathsf{T}} \cdot \boldsymbol{R} \, \mathrm{d}A = \delta \boldsymbol{\Phi}^{\mathsf{T}} \boldsymbol{K} \boldsymbol{\Phi}, \quad \boldsymbol{K} = \int_A \boldsymbol{B}^{\mathsf{T}} \boldsymbol{H}_T \boldsymbol{B} \, \mathrm{d}A \tag{40}$$

where $\boldsymbol{K}$ is the global stiffness matrix.

Therefore, the discretized static linear piezoelastic equilibrium equation for the structure can be written as

$$\boldsymbol{K} \boldsymbol{\Phi} = \boldsymbol{F} \tag{41}$$

where $\boldsymbol{F}$ is the contribution of either the internal and the external works.

3.4. Nodal transformation

The variation of the directors $\delta \boldsymbol{d}$ and their derivatives $\delta \boldsymbol{d}_{,\alpha}$ can be expressed either in spatial description, in all equations,

$$\delta \boldsymbol{d} = \delta \boldsymbol{\theta} \wedge \boldsymbol{d} = \boldsymbol{\Lambda} \delta \boldsymbol{\theta}, \quad \bar{\boldsymbol{\Lambda}} = -\tilde{\boldsymbol{d}} \tag{42}$$

where $\tilde{\boldsymbol{d}}$ is a skew-symmetric tensor such that $\tilde{\boldsymbol{d}} \boldsymbol{d} = \boldsymbol{0}$, or in material description,

$$\delta \boldsymbol{d} = \boldsymbol{Q} \, \delta \overline{\boldsymbol{\Theta}} \boldsymbol{E}_3 = \bar{\boldsymbol{\Lambda}} \delta \boldsymbol{\Theta}, \quad \bar{\boldsymbol{\Lambda}} = \boldsymbol{Q} \, \tilde{\boldsymbol{E}}_3 \tag{43}$$

where $\boldsymbol{d} = \boldsymbol{Q}\,\boldsymbol{E}_3$, $\boldsymbol{E}_3 = [\,0 \quad 0 \quad 1\,]^t$ and $\boldsymbol{Q} = [\,\boldsymbol{t}_1 \quad \boldsymbol{t}_2 \quad \boldsymbol{t}_3\,]$.

A spatial description leads to a shell problem with 7 DOF/node, and the material description leads to a shell problem with 6 DOF/node. The transformation $\bar{\boldsymbol{\Lambda}}$ takes the following form:

$$\bar{\boldsymbol{\Lambda}}_n = [\,-\boldsymbol{t}_{2n} \quad \boldsymbol{t}_{1n}\,]_{3\times 2}, \quad n = 1, \ldots, 4 \tag{44}$$

The relation between the generalized displacement vector $\delta\boldsymbol{\Phi}_n = (\delta\boldsymbol{x}, \delta\boldsymbol{d}, \delta\varphi)_n$ and the nodal displacement $\delta\boldsymbol{\Gamma}_n = (\delta\boldsymbol{x}, \delta\boldsymbol{\Theta}, \delta\varphi)_n$ vectors is defined as:

$$\delta\boldsymbol{\Phi}_n = \boldsymbol{\Pi}_n\delta\boldsymbol{\Gamma}_n, \quad n = 1, \ldots, 4 \tag{45}$$

where $\boldsymbol{\Pi}_n = \begin{bmatrix} \boldsymbol{I} & \boldsymbol{0} & 0 \\ \boldsymbol{0} & \Lambda_{\bar{n}} & 0 \\ 0 & 0 & 1 \end{bmatrix}$.

The global stiffness matrix becomes:

$$\boldsymbol{K}_T = \boldsymbol{\Pi}^{\mathsf{T}}\boldsymbol{K}\boldsymbol{\Pi} \tag{46}$$

where $\boldsymbol{\Pi} = \mathrm{diag}(\boldsymbol{\Pi}_1, \boldsymbol{\Pi}_2, \boldsymbol{\Pi}_3, \boldsymbol{\Pi}_4)$.

The discretized static linear piezoelastic equilibrium equation becomes:

$$K_T\boldsymbol{\Gamma} = F \tag{47}$$

4. Material properties of FGM shell

The studied FGM shell structure is made of two kinds of materials, and its properties are assumed to vary continuously throughout the direction of the thickness (z-axis), according to a power function of the volume fractions of the constituents. Based on the power-law model of Bao and Wang [43], the volume fraction of the upper material V_u can be considered as:

$$V_u(z) = \left(\frac{z}{h} + \frac{1}{2}\right)^n \tag{48}$$

where $z \in [-\frac{h}{2}, \frac{h}{2}]$, h the thickness of the structure, and the exponent n is the power-law index (volume fraction exponent), which represents the gradation of material properties across the direction of the thickness. The volume fraction of the upper constituent is associated with that of the lower constituent using the following relation:

$$V_{\mathrm{u}}(z) + V_{\mathrm{l}}(z) = 1 \tag{49}$$

The subscripts u and l denote the upper and lower constituents, respectively.

The effective material properties of FGM can be expressed as:

$$P_{\mathrm{eff}}(T, z) = P_{\mathrm{ul}}(T)V_{\mathrm{u}}(z) + P_{\mathrm{l}}(T), \quad P_{\mathrm{ul}}(T) = P_{\mathrm{u}} - P_{\mathrm{l}} \tag{50}$$

where P_{u} and P_{l} denote respectively the properties of the upper and lower materials such as Young's modulus Y. Functionally gradient materials are mainly used in high-temperature environments, the material properties are expressed as functions of temperature, as given by Touloukian [44], in the form:

$$P(T) = P_0\left(P_{-1}T^{-1} + 1 + P_1T + P_2T^2 + P_3T^3\right) \tag{51}$$

where P_0, P_{-1}, P_1, P_2, and P_3 are the temperature coefficients. In this paper, the Young modulus is considered as temperature dependent. The Poisson ratio ν is constant through the direction of the thickness.

5. Numerical results

So far, there are no theoretical, experimental, and numerical results on the behavior of active materials integrated into an FGM passive structure available in the existing literature to which we can compare our model. Therefore, in order to demonstrate the efficiency of the present model, comparisons are carried out for different cases reported in the literature and using isotropic shell structures with integrated piezoelectric materials.

First, before the electromechanical behavior of the piezolaminated structure composed of piezoelectric patches bonded to the FGM surface is investigated, three illustrative examples are examined to ensure the accuracy and validity of the developed Kirchhoff model: (i) clamped beam with active piezoelectric layers; (ii) active plate structure; (iii) simply supported composite cylindrical arch.

Then, the numerical results of the study of the electromechanical coupling behavior of a thin-walled active structure with a laminate architecture featuring an FGM composite as a passive material and utilizing piezoelectric patches as both sensor and actuator components are presented.

Table 2
Electromechanical material properties.

Material properties	Aluminum	Steel	T300/976	PIC 151	PZT G1195
Elastic properties					
Elastic modulus Y_{11} (GPa)	70.3	207	150	59.4	63
Elastic modulus Y_{22} (GPa)	70.3	207	9	59.4	63
Poisson's ratio ν_{12}	0.33	0.28	0.3	0.38	0.3
Piezoelectric properties					
Piezoelectric coupling coefficient e_{31} (C·m^{-2})	0	0	0	9.6	2.286
Piezoelectric coupling coefficient e_{32} (C·m^{-2})	0	0	0	9.6	2.286
Dielectric permittivity coefficient d_{33} (F·m^{-1})	0	0	0	1.71e−8	1.5e−8
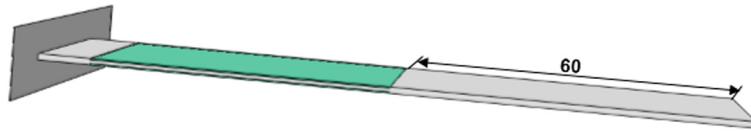
Fig. 4. Geometry of the beam with active piezoelectric layers.

Three different configurations according to the location of the piezo active layers bonded on the top and the bottom of the structure are investigated to show the applicability and the versatility of the linear discrete Kirchhoff model. The influence of the geometrical parameters and of the power-law index on the response of the piezolaminated structure are also examined. The electromechanical material properties of all the materials used in this section are listed in Table 2 according to [34,39,41].

5.1. Comparison studies

5.1.1. Clamped beam with active piezoelectric layers
This example consists of a clamped beam made of aluminum with a pair of piezo patches bonded to its upper and lower surfaces, as shown in Fig. 4. The geometry of the structure is taken according to Marinkovic et al. [34], where $L = 110$ mm is the axial length, $b = 27.5$ mm is the width, and $h = 0.5$ mm is the thickness of the structure.

The pair of patches (PIC151) have dimensions $a \times b = 42.5 \times 27.5$ mm as depicted in Fig. 4. The thickness of each active layer is $h = 0.2$ mm. The material properties are listed in Table 2.

A voltage of 100 V is applied between the electrodes of the patches. Due to the opposite polarization of the patches, their activation produces internal bending moments uniformly distributed over the edges of the patches. Table 3 and Fig. 5 present a comparison of the static deflection of the centerline of the beam obtained using the present model, the ACShell9 user element developed in [34], and the ABAQUS standard piezoelectric element C3D20E.

As may be seen, the present results are in good agreement with those obtained using the ACShell9 user element and ABAQUS C3D20E element. Hence, the present model can accurately predict the static deflection of the piezolaminated beam subjected to an electric voltage of 100 V applied to the piezo patches.

Table 4 tabulates the effect of the voltage change V on the stress σ_{xx} at point $(0, b/2, 0)$ of the clamped beam with active piezoelectric layers. The stress at central point of the clamped beam with active piezoelectric layers rises with increasing voltage.

5.1.2. Active plate structure
The structure tested in this section is an active steel plate clamped over all four edges. Four pairs of collocated piezoelectric actuators (PIC151) of thickness 0.2 mm are attached to the lower and upper surfaces of the plate. The thickness of the plate is 1 mm. The geometry of the studied piezolaminated plate is illustrated in Fig. 6. The material properties of the steel and of the PIC 151 are given in Table 2. The patches of each side are oppositely polarized, whereby all the patches on one side of the plate have the same polarization. The symmetry of the model allows the consideration of only one quarter of the plate for the FE simulation. The quarter of the plate is discretized by 40×60 elements along the width and axial directions, respectively.

Since the piezolayers are oppositely polarized, when the active plate is exposed to the same electric voltage of 100 V, it is supplied to both of them simultaneously, a bending moment uniformly distributed over the edges is induced, and a static deflection of the plate occurs.

Comparisons of static centerline deflection considering one quarter of the piezolaminated plate acquired using the present model, UEL subroutine developed by Nestorovic et al. [41] and Abaqus standard piezoelectric hexahedral element C3D20E, when the active plate is exposed to electric voltage of 100 V, are shown in Table 5 and in Fig. 7. It can be noticed that excellent agreement is achieved between the present results and the numerical solutions. Further, stresses at the central point $(a/2, b/2, 0)$ of the active plate rises with increasing voltage, as listed in Table 6.

Table 3
Deflections of the clamped beam with active piezoelectric layers.

Distance (mm)	Deflections (mm)		
	Present model	Marinkovic et al. [34]	Abaqus C3D20E
0	0	0	0
15	−0.002	−0.007	−0.007
30	−0.040	−0.042	−0.042
45	−0.119	−0.122	−0.122
60	−0.229	−0.233	−0.233
75	−0.34	−0.347	−0.347
90	−0.453	−0.460	−0.460
110	−0.601	−0.610	−0.610
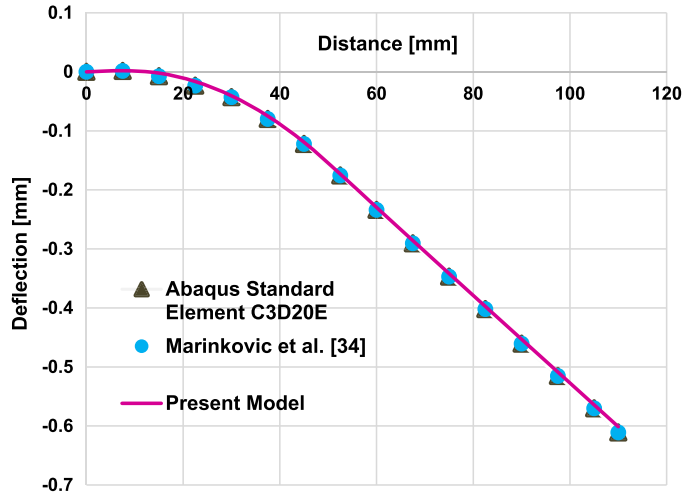
Fig. 5. Comparison of the static deflection of the centerline of the piezolaminated beam subjected to an electric voltage of 100 V.

Table 4
Effect of voltage change on the stresses at the central point of the clamped beam with active piezoelectric layers.

	10 V	50 V	100 V	200 V	300 V
σ_{xx} $(0, b/2, 0)$ (MPa)	0.120	0.604	1.207	2.415	3.622
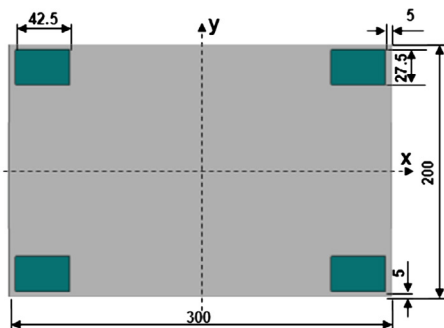
(a) Geometrical parameters of the active plate.
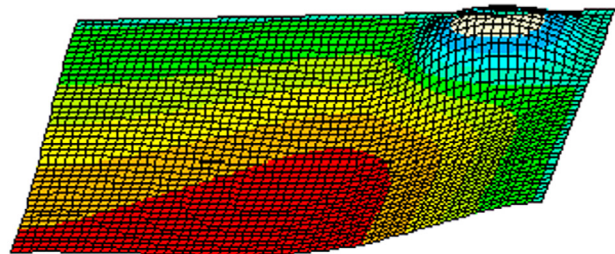
(b) Deflection of a quarter of the plate

Fig. 6. Geometry of the active plate clamped at all edges.

5.1.3. Simply supported composite cylindrical arch

This example consists of a simply supported cylindrical arch made of composite T300/976 with continuous PZT G1195 actuators embedded on the top and the bottom of the composite surface as shown in Fig. 8. The piezolaminated structure has been modeled using a standardized 4×40 mesh along the axial and circumferential directions, respectively. The stacking sequence of the composite is $[45/-45/0]$ s. The electro-elastic properties of materials are shown in Table 2. Each composite

Table 5
Centerline deflection considering one quarter of the active plate.

Distance (mm)	Deflections (mm)		
	Present model	Nestorovic et al. [41]	Abaqus C3D20E
0	0	0	0
40	−2.050	−2.030	−2.090
60	−3.024	−3.016	−3.017
80	−3.371	−3.302	−3.389
100	−3.260	−3.117	−3.231
130	−2.874	−2.752	−2.873
150	−2.770	−2.666	−2.795
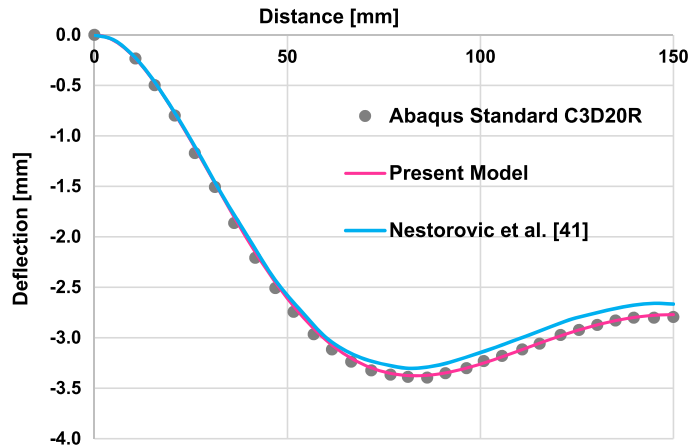
Fig. 7. Centerline deflection considering one quarter of the plate, $y = 0$.

Table 6
Effect of voltage change on the stresses at the central point of the active plate.

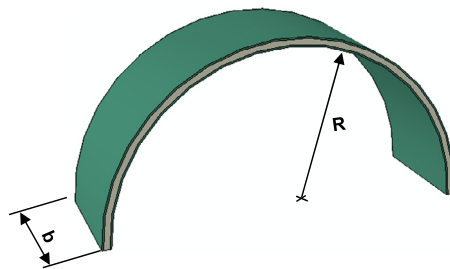|	10 V	50 V	100 V	200 V	300 V
σ_{xx} $(a/2, b/2, 0)$ (MPa)	2.001e−3	1.280e−2	2.561e−2	5.122e−2	7.684e−2

Fig. 8. Simply supported piezo active composite cylindrical arch.

ply is 0.12 mm in thickness, and the thickness of each piezoelectric layer is 0.24 mm. The radius of cylindrical arch is $R = 100$ mm, and the axial length is $b = 60$ mm.

The considered cylindrical arch is excited by the actuation of the piezolayers. The oppositely polarized layers are subjected to a voltage of 100 V. A comparison of numerical results of the radial deflection at the width mid-line obtained using the present approach and the Shell9 user element implemented by Marinkovic et al. [39] has been conducted, as illustrated in Table 7 and in Fig. 9.

Again, the present results are in excellent concordance with the numerical ones given by Marinkovic et al. [39]. Hence, the proposed piezoelectric Kirchhoff shell developed in the present study shows a good ability to predict the linear behavior of various active structures with good accuracy.

The influence of the electric potential variation on the maximal stresses of the simply supported piezo active composite cylindrical arch is examined in Table 8. Table 9 shows the effect of the variation of the slenderness ratio R/h_{tot} on the maximal stresses considering $V = 100$ V. h_{tot} denotes the full thickness of the structure.

Table 7
Radial deflection of simply supported active composite arch.

Distance (mm)	Deflections (mm)	
	Present model	Marinkovic et al. [39]
0	0	0
0.1	0.075	0.089
0.2	0.052	0.050
0.3	−0.013	−0.029
0.4	−0.075	−0.092
0.5	−0.100	−0.116
0.6	−0.075	−0.089
0.7	−0.013	−0.018
0.8	0.052	0.058
0.9	0.075	0.088
1	0	0
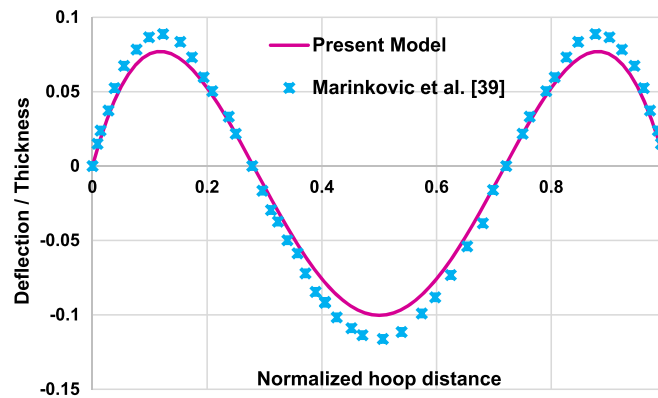
Fig. 9. Radial deflection of a piezo active composite arch.

Table 8
Effect of voltage change on the maximal stresses of the simply supported piezo arch.

	10 V	50 V	100 V	200 V	300 V
σ_{max} (MPa)	2.544	12.720	25.440	50.881	76.321

Table 9
Effect of the slenderness ratio variation on the maximal stress of the simply supported piezo arch.

R/h_{tot}	20	50	100	150	200
σ_{max} (MPa)	5.818	14.729	30.748	46.576	67.244

5.2. FGM active plate analysis

After the validation of the current linear formulation, the electromechanical behavior of thin-walled active structure with a laminate architecture featuring an FGM composite as a passive material and utilizing piezoelectric patches as both sensor and actuator components is now examined based on the developed piezoelectric Kirchhoff shell.

A piezolaminated FGM active plate with four pairs of G-1195N piezoelectric patches attached to the top and the bottom surfaces of the structure is investigated. The geometry of the plate is the same as that illustrated in Fig. 6. The patches of each pair are oppositely polarized, whereby all the patches on one side of the plate have the same polarization. The actuation of the patches is achieved by simultaneously applying the same voltage of 100 V to each of them.

The FGM plate is composed of two materials, Ti–6Al–4V and aluminum, and its properties are graded in the direction of the thickness according to the volume power-law fraction distribution presented in Eq. (48). The inversely polarized piezo active patches are bonded on the top and the bottom surfaces of the structure, considering various location configurations A, B, and C, as depicted in Fig. 10. The shell laminate is discretized into a uniform mesh of 140 (14×10) elements. The thickness of the FGM plate is 1 mm and each G-1195N patch is 0.2 mm in thickness. The material properties of the G-1195N patch and of the FGM plate are listed in Table 10. The top surface of the FGM shell is assumed to be "Ti–6Al–4V rich", while the bottom surface is "aluminum rich" for all considered location configurations (A, B, and C).

(a) Configuration A   (b) Configuration B   (c) Configuration C
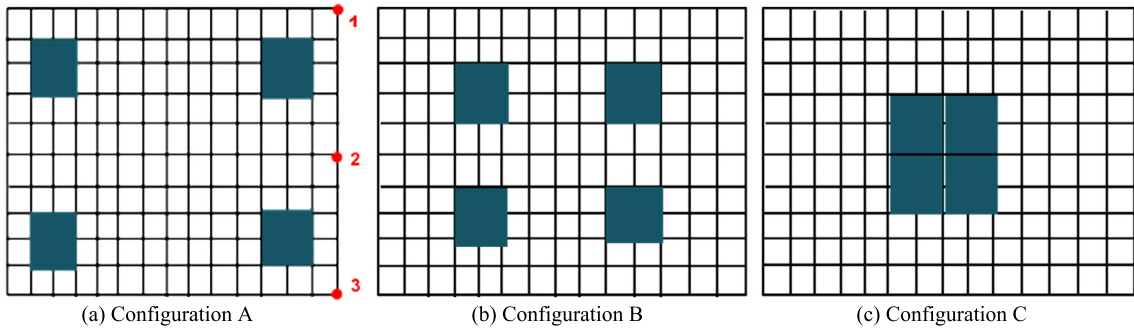
Fig. 10. A schematic diagram showing the various configurations of the piezoelectric patches.

Table 10
Materials constants of the constituent materials of the FGM after He et al. [45].

Material constants	Aluminum oxide			Ti–6Al–4V		
	Y (Pa)	ν	ρ (kg·m^{-3})	Y (Pa)	ν	ρ (kg·m^{-3})
P_0	349.55e9	0.26	3750	122.56e9	0.2884	4429
P_{-1}	0	0	0	0	0	0
P_1	−3.853e−4	0	0	−4.586e−4	1.1211e−4	0
P_2	4.027e−7	0	0	0	0	0
P_3	−1.673e−10	0	0	0	0	0

In all the considered cases, the active layers have symmetric position with respect to the thickness of the structure, and they act as actuators. They are oppositely polarized and supplied with the same electric voltage of 100 V, which results in bending moments uniformly distributed over the edges of the surface covered by piezopatches, which results in bending-dominated behavior of the structure.

Firstly, the bending-dominated behavior of the laminated plate containing the active piezoelectric layers is investigated according to configuration A.

The longitudinal bending W_L, the transverse bending W_T, and the lateral twisting W_R are defined as in [46]:

$$W_L = \frac{W_2}{b}, \qquad W_T = \frac{W_2 - (W_1 + W_3)/2}{b}, \qquad W_R = \frac{W_1 - W_3}{b} \tag{52}$$

where b is the width of the plate and W_1, W_2 and W_3 are the lateral deflections at locations shown in Fig. 10a.

In order to illustrate the influence of the volume fraction exponent on the static response of the piezolaminated structure, the variation of the longitudinal bending, transverse bending, and lateral twisting are tabulated in Tables 11, 12 and 13, and plotted in Figs. 11, 12, and 13, respectively, for different values of the volume fraction exponent.

Furthermore, the effect of the volume fraction exponent on normal stresses along the thickness of the plate (configuration A) subjected to a voltage of 100 V are presented in Figs. 14 and 15 and tabulated in Tables 14 and 15.

It can be obviously observed that the volume fraction exponent has a significant effect on the behavior of the active plate subjected to a uniform voltage. In fact, an increase in the volume fraction exponent leads to a decrease of the deflections. This is because the mechanically induced deformation mainly depends on the bending stiffness of the actuator, and an increase in the volume fraction exponent leads to a greater amount of aluminum, which has higher elastic material properties compared to Ti–6Al–4V; therefore, its bending stiffness is greater.

To highlight the effect of the disposition of the patches on the static responses of the FGM shell laminate with distributed piezoelectric sensor and actuator pairs, static deflections are examined according to the configurations A, B, and C represented in Fig. 10. The actuation of the patches is achieved by simultaneously applying the same voltage of 100 V to each of them.

Only one quarter of the plate is considered for the simulation because of the symmetry of the model. Tables 16–18, and Figs. 16–18 show a centerline deflection, considering one quarter of the plate for the different location configurations of the piezo active layers A, B, and C, considering the effect of various values of the volume fraction index.

As can be seen, in a fashion similar to the previous example, the volume fraction index has an important influence on the static response of the active FGM structure. Indeed, with the increase of the volume fraction exponent n, the static deflections of FGM plate decrease in all configurations.

Hence, the highest deflections in all the proposed configurations are obtained considering the volume fraction exponent $n = 0$. Table 19 reports the maximum centerline deflections obtained for configurations A, B, and C, $y = 0$, considering the volume fraction exponent $n = 0$. It can be noticed that varied values of maximum centerline deflections are obtained, corresponding to each configuration.

It is also observed that the static behavior of the piezolaminated FGM structure is different from one configuration to the other. This reveals the existence of an optimal location of the piezoelectric patch with respect to the objective of achieving

Table 11

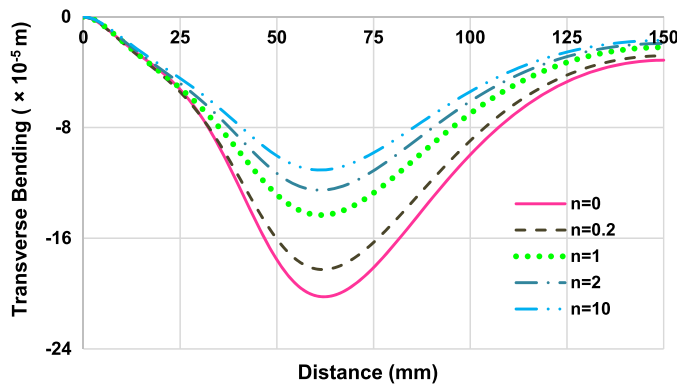Longitudinal bending of clamped FGM plate for various volume fraction indexes.

Distance (mm)	Longitudinal bending (10^{-5} m)				
	$n = 0$	$n = 0.2$	$n = 1$	$n = 2$	$n = 10$
0	0	0	0	0	0
25	−1.416	−1.357	−1.168	−1.057	−0.959
50	−4.019	−3.665	−2.927	−2.578	−2.293
75	−4.762	−4.303	−3.392	−2.975	−2.639
100	−3.913	−3.532	−2.781	−2.439	−2.164
125	−3.104	−2.801	−2.204	−1.934	−1.715
150	−2.811	−2.536	−1.995	−1.750	−1.553
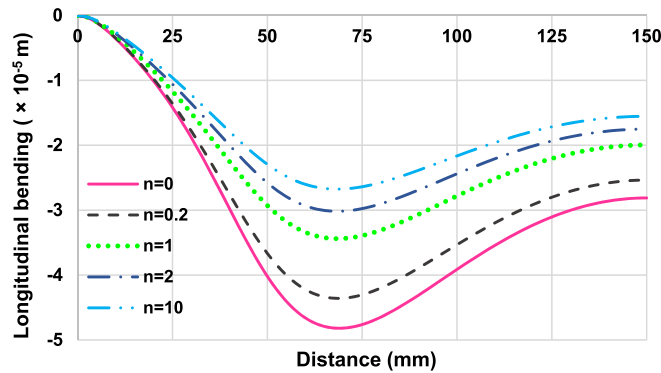
Fig. 11. Longitudinal bending of the clamped FGM plate for various volume fraction indexes.

Table 12

Transverse bending of clamped FGM plate for various volume fraction indexes.

| Distance (mm)	Transverse bending (10^{-5} m)				
	$n = 0$	$n = 0.2$	$n = 1$	$n = 2$	$n = 10$
0	0	0	0	0	0
25	−5.250	−5.437	−5.161	−4.813	−4.449
50	−17.555	−16.061	−12.852	−11.313	−10.045
75	−18.122	−16.302	−12.732	−11.121	−9.826
100	−9.966	−8.955	−6.993	−6.112	−5.406
125	−4.694	−4.217	−3.296	−2.883	−2.552
150	−3.139	−2.820	−2.205	−1.929	−1.709

Fig. 12. Transverse bending of clamped FGM plate for various volume fraction indexes.

the intended response. In fact, a piezolaminated composite with distributed piezosensors and actuators enables the structure to respond in real time or nearly real time to external stimuli to compensate for undesired behavior or to produce a desired response.

The multilayered material including piezoelectric active layers is polarized in the direction of the thickness. Hence, it is important to investigate the influence of the thickness of the piezoelectric layer on the deformation of the laminated

Table 13
Lateral twisting of clamped FGM plate for various volume fraction indexes.

Distance (mm)	Lateral twisting (10^{-5})				
	$n = 0$	$n = 0.2$	$n = 1$	$n = 2$	$n = 10$
0	0	0	0	0	0
25	1.782	1.626	1.305	1.153	1.028
50	4.528	4.118	3.283	2.894	2.577
75	5.901	5.347	4.238	3.727	3.312
100	5.833	5.273	4.163	3.657	3.247
125	5.270	4.758	3.750	3.291	2.920
150	4.995	4.508	3.550	3.115	2.764
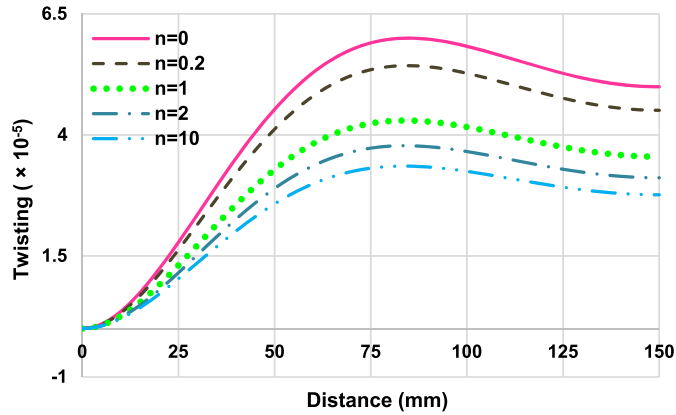
Fig. 13. Lateral twisting of a clamped FGM plate for various values of the volume fraction index.

Table 14
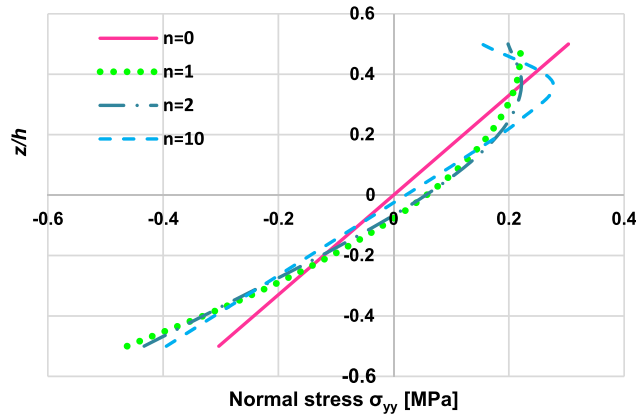Normal stress σ_{xx} for various values of the volume fraction exponent.

σ_{xx} (0.0.z) (MPa)				
z/h	$n = 0$	$n = 1$	$n = 2$	$n = 10$
-0.5	0.075	0.120	0.114	0.107
-0.375	0.056	0.074	0.078	0.078
-0.25	0.037	0.035	0.043	0.050
-0.125	0.018	0.004	0.009	0.021
0	5.472e-17	-0.020	-0.019	-0.007
0.125	-0.018	-0.038	-0.042	-0.035
0.25	-0.037	-0.051	-0.055	-0.061
0.375	-0.056	-0.057	-0.059	-0.075
0.5	-0.075	-0.057	-0.051	-0.038
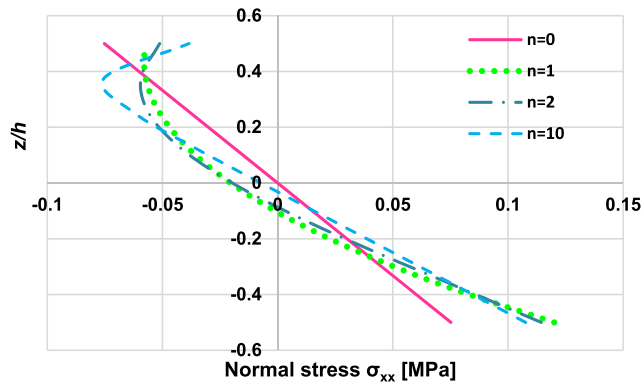
Fig. 14. Normal stress σ_{xx} (0.0.z) for various values of the volume fraction exponent.

Table 15

Normal stress σ_{yy} for various values of the volume fraction exponent.

σ_{yy} (0.0.z) (MPa)				
z/h	$n = 0$	$n = 1$	$n = 2$	$n = 10$
−0.5	−0.303	−0.462	−0.432	−0.394
−0.375	−0.227	−0.299	−0.304	−0.291
−0.25	−0.151	−0.15	−0.175	−0.186
−0.125	−0.075	−0.039	−0.052	−0.082
0	3.072e−17	0.057	0.055	0.021
0.125	0.075	0.131	0.143	0.124
0.25	0.151	0.183	0.201	0.220
0.375	0.227	0.213	0.221	0.275
0.5	0.303	0.221	0.198	0.153

Fig. 15. Normal stress σ_{yy} (0.0.z) for various values of the volume fraction exponent.

Table 16

Centerline deflection considering one quarter of the plate under various values of the volume fraction index (configuration A), $y = 0$.

| Distance (mm)	Centerline deflection (10^{-6} m)				
	$n = 0$	$n = 0.2$	$n = 1$	$n = 2$	$n = 10$
0	0	0	0	0	0
25	−5.139	−4.366	−3.078	−2.576	−2.202
50	−12.834	−10.889	−7.660	−6.405	−5.472
75	−16.454	−13.942	−9.789	−8.179	−6.985
100	−16.102	−13.635	−9.565	−7.990	−6.823
125	−14.476	−12.255	−8.594	−7.179	−6.130
150	−13.697	−11.595	−8.131	−6.792	−5.799
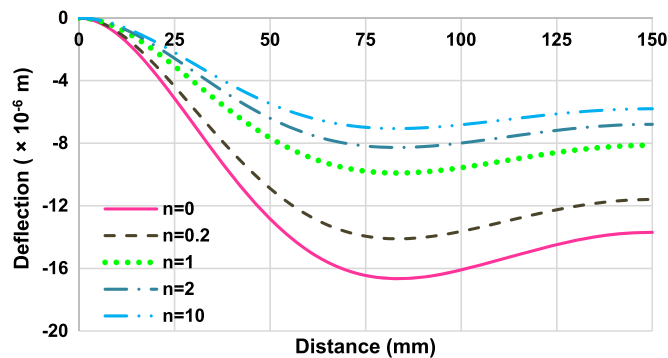
Fig. 16. Centerline deflection considering one quarter of the plate under various values of the volume fraction index (configuration A), $y = 0$.

Table 17

Centerline deflection considering one quarter of the plate under various values of the volume fraction index (configuration B), $y = 0$.

Distance (mm)	Centerline deflection (10^{-6} m)				
	$n = 0$	$n = 0.2$	$n = 1$	$n = 2$	$n = 10$
0	0	0	0	0	0
25	−3.0098	−2.566541	−1.826024	−1.535045	−1.317258
50	−10.9043	−9.265755	−6.554881	−5.49844	−4.710843
75	−14.8663	−12.59769	−8.872772	−7.430347	−6.358237
100	−7.6735	−6.537586	−4.646912	−3.905633	−3.351197
125	2.2070	1.843149	1.263963	1.046673	0.8879524
150	6.1420	5.196355	3.646979	3.049101	2.605748
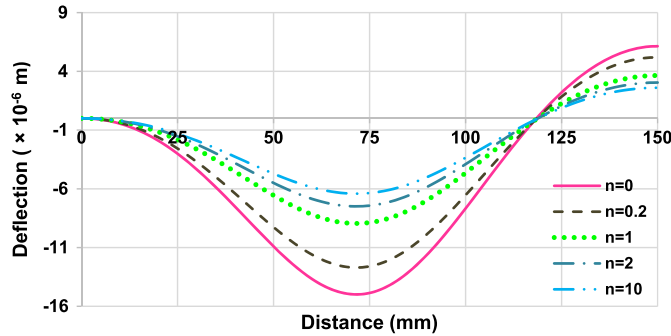
Fig. 17. Centerline deflection considering one quarter of the plate under various values of the volume fraction index (configuration B), $y = 0$.

Table 18

Centerline deflection considering one quarter of the plate under various values of the volume fraction index (configuration C), $y = 0$.

Distance (mm)	Centerline deflection (10^{-5} m)				
	$n = 0$	$n = 0.2$	$n = 1$	$n = 2$	$n = 10$
0	0	0	0	0	0
25	−0.2533	−0.2242	−0.1688	−0.1449	−0.1262
50	−1.2302	−1.0787	−0.8013	−0.6843	−0.5940
75	−3.5456	−3.0870	−2.2687	−1.9301	−1.6707
100	−8.1718	−7.0843	−5.1717	−4.3891	−3.7925
125	−12.6269	−10.9264	−7.9535	−6.7426	−5.8214
150	−13.0679	−11.3237	−8.2607	−7.0089	−6.0549
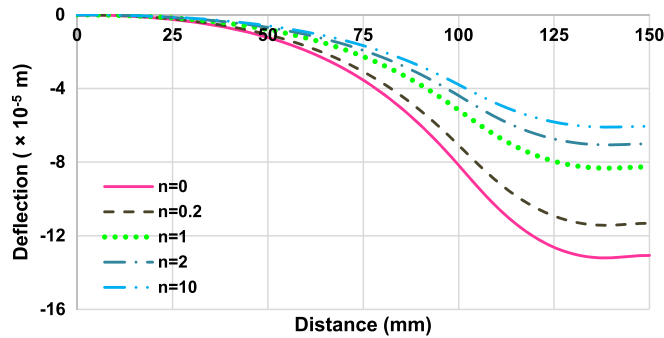
Fig. 18. Centerline deflection considering one quarter of the plate under various values of the volume fraction index (configuration C), $y = 0$.

structure. Table 20 and Fig. 19 show the effect of the slenderness ratio a/h on the centerline deflection of the active FGM plate under a uniform potential of 100 V for a volume fraction index $n = 2$ (configuration A).

It was found that the centerline deflection of the FGM plate increases as the slenderness ratio rises. This implies that piezoelectric layer thickness has a significant effect on the piezoelastic linear behavior of the active structure. Such sensitive geometrical parameter should be carefully considered for the design of smart structures with integrated piezoelectric patches.

Table 19

Maximum deflections obtained for configurations A, B and C considering the volume fraction exponent $n = 0$.

Maximum deflections (m)		
Configuration A	Configuration B	Configuration C
$-16.65\text{e}{-6}$	$-15.00\text{e}{-6}$	$-13.2\text{e}{-5}$

Table 20

Centerline deflection considering one quarter of the plate under various values of the piezoelectric layer thickness (configuration A), $y = 0$ and $n = 2$.

Distance (mm)	Centerline deflection (10^{-6} m)				
	$a/h = 250$	$a/h = 300$	$a/h = 400$	$a/h = 500$	$a/h = 1000$
0	0	0	0	0	0
25	-2.4392	-2.5767	-2.0404	-1.8127	-2.3068
50	-6.0995	-6.4050	-5.1549	-4.6061	-5.7893
75	-7.8287	-8.1799	-6.6805	-6.0036	-7.4550
100	-7.6664	-7.9908	-6.5799	-5.9349	-7.3141
125	-6.8938	-7.1794	-5.9338	-5.3630	-6.5828
150	-6.5234	-6.7924	-5.6201	-5.0828	-6.2307
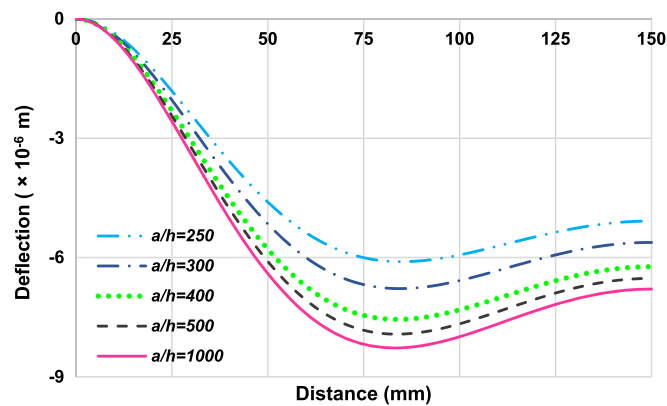
Fig. 19. Effect of the piezoelectric layer thickness on the centerline deflection considering one quarter of the plate, $y = 0$, subjected to an electric voltage of 100 V (configuration A).

6. Conclusions

Piezoelectric patches become more and more frequently utilized as active elements on thin-walled structures as both sensor and actuator components. Hence, the analysis of thin-walled structures with embedded active piezoelectric elements is of increasing importance. This was a motivation for publishing the current investigation, which considers closely the actual distribution of electric potential and electric field across the thickness of active elements, taking into account kinematical assumptions. The analysis of static deflections of thin-walled active structures with laminate architecture featuring passive material and utilizing piezoelectric patches is presented using a discrete form of Kirchhoff's finite element model. The approximation of the displacement field is carried out using four-node finite elements. The current approach allows two aspects of analysis: computational and application sides. On the computational aspect, the present model constitutes an alternative to the examination of the electromechanical coupling behavior of piezolaminated structures without locking problems and with low computational effort. On the application aspect, the proposed piezoelectric Kirchhoff finite element model extend the numerical framework to advanced applications of smart structures; indeed, the element covers the modeling of arbitrary thin-walled structures with complex geometries and involving functionally graded materials. The performance and the accuracy of the presented model are highlighted through numerical examples with different geometries. Finally, the developed piezoelectric Kirchhoff model shows good ability to predict the linear behavior of piezolaminated FGM structures for various location configurations of the piezoelectric patches. It was found that the power-law index and the piezoelectric layer thickness have significant effects on the static response of the piezolaminated FGM structure.

References

[1] M.V. Gandhi, B.S. Thompson, Smart Materials and Structures, Chapman & Hall, London, 1992.

[2] U. Gabbert, Research activities in smart materials and structures and expectations to future developments, J. Theor. Appl. Mech. 3 (43) (2002) 549–574.

[3] W.M. Zhang, G. Meng, D. Chen, Stability, nonlinearity and reliability of electrostatically actuated MEMS devices, Sensors 7 (5) (2007) 760–796.

[4] M.A. Foda, A.A. Almajed, M.M. ElMadany, Vibration suppression of composite laminated beams using distributed piezoelectric patches, Smart Mater. Struct. 19 (11) (2010) 115018.

[5] J.M. Dietl, A.M. Wickenheiser, E.A. Garcia, Timoshenko beam model for cantilevered piezoelectric energy harvesters, Smart Mater. Struct. 19 (5) (2010) 055018.

[6] S. Chesne, C. Pezerat, Distributed piezoelectric sensors for boundary force measurements in Euler–Bernoulli beams, Smart Mater. Struct. 20 (7) (2011) 075009.

[7] W.M. Zhang, O. Tabata, T. Tsuchiya, G. Meng, Noise-induced chaos in the electrostatically actuated MEMS resonators, Phys. Lett. A 375 (32) (2011) 2903–2910.

[8] N. Kammoun, H. Jrad, S. Bouaziz, M.B. Amar, M. Soula, M. Haddar, Thermo-electro-mechanical vibration characteristics of graphene/piezoelectric/graphene sandwich nanobeams, J. Mech. (2017) 1–15, https://doi.org/10.1017/jmech.2017.89.

[9] W. Pompea, H. Worch, M. Epple, W. Friess, M. Gelinsky, P. Greil, U. Hempele, D. Scharnweber, K. Schulte, Functionally graded materials for biomedical applications, Mater. Sci. Eng. A 362 (2003) 40–60.

[10] E. Müller, C. Drašar, J. Schilz, W.A. Kaysser, Functionally graded materials for sensor and energy applications, Mater. Sci. Eng. 362 (2003) 17–30.

[11] A. Kidane, A. Shukla, Dynamic constitutive behavior of Ti/TiB FGM under thermo mechanical loading, J. Mater. Sci. 43 (2008) 2771–2777.

[12] J.N. Reddy, C.F. Liu, A higher-order shear deformation theory of laminated elastic shells, Int. J. Eng. Sci. 23 (3) (1985) 319–330.

[13] L. Dozio, On the use of the trigonometric Ritz method for general vibration analysis of rectangular Kirchhoff plates, Thin-Walled Struct. 49 (1) (2011) 129–144.

[14] J.N. Reddy, D.H. Robbins, Theories and computational models for composite laminates, Appl. Mech. Rev. 47 (6) (1994) 147–169.

[15] A.J.M. Ferreira, G.E. Fasshauer, R.C. Batra, J.D. Rodrigues, Static deformations and vibration analysis of composite and sandwich plates using a layerwise theory and RBF-PS discretizations with optimal shape parameter, Compos. Struct. 86 (4) (2008) 328–343.

[16] E. Carrera, S. Brischetto, P. Nali, Plates and Shells for Smart Structures: Classical and Advanced Theories for Modeling and Analysis, 1st edition, John Wiley and Sons, Ltd, 2011.

[17] M. Cinefra, E. Carrera, L. Della Croce, C. Chinosi, Refined shell elements for the analysis of functionally graded structures, Compos. Struct. 94 (2) (2012) 415–422.

[18] E. Viola, F. Tornabene, N. Fantuzzi, Static analysis of completely doubly-curved laminated shells and panels using general higher-order shear deformation theories, Compos. Struct. 101 (2013) 59–93.

[19] E. Viola, F. Tornabene, N. Fantuzzi, General higher-order shear deformation theories for the free vibration analysis of completely doubly-curved laminated shells and panels, Compos. Struct. 95 (2013) 639–666.

[20] F. Tornabene, E. Viola, Static analysis of functionally graded doubly-curved shells and panels of revolution, Meccanica 48 (4) (2013) 901–930.

[21] J.N. Reddy, A.R. Srinivasa, Non-linear theories of beams and plates accounting for moderate rotations and material length scales, Int. J. Non-Linear Mech. 66 (2014) 43–53.

[22] Y.Q. Tang, Z.H. Zhou, S.L. Chan, Geometrically nonlinear analysis of shells by quadrilateral at shell element with drill, shear, and warping, Int. J. Numer. Methods Eng. 108 (10) (2016) 1248–1272.

[23] J. Mars, S. Koubaa, M. Wali, F. Dammak, Numerical analysis of geometrically non-linear behavior of functionally graded shells, Lat. Am. J. Solids Struct. 14 (11) (2017) 1952–1978.

[24] A. Frikha, M. Wali, A. Hajlaoui, F. Dammak, Dynamic response of functionally graded material shells with a discrete double directors shell element, Compos. Struct. 154 (2016) 385–395.

[25] A. Frikha, F. Dammak, Geometrically nonlinear static analysis of functionally graded material shells with a discrete double directors shell element, Comput. Methods Appl. Mech. Eng. 315 (2017) 1–24.

[26] S. Zghal, A. Frikha, F. Dammak, Free vibration analysis of carbon nanotube-reinforced functionally graded composite shell structures, Appl. Math. Model. 53 (2018) 132–155.

[27] S. Zghal, A. Frikha, F. Dammak, Static analysis of functionally graded carbon nanotube-reinforced plate and shell structures, Compos. Struct. 176 (2017) 1107–1123.

[28] C. Miehe, A theoretical and computational model for isotropic elastoplastic stress analysis in shells at large strains, Comput. Methods Appl. Mech. Eng. 155 (3–4) (1998) 193–233.

[29] S. Klinkel, F. Gruttmann, W. Wagner, A robust non-linear solid shell element based on a mixed variational formulation, Comput. Methods Appl. Mech. Eng. 195 (2006) 179–201.

[30] M. Schwarze, S. Reese, A reduced integration solid-shell finite element based on the EAS and the ANS concept-large deformation problems, Int. J. Numer. Methods Eng. 85 (3) (2011) 289–329.

[31] K. Rah, W. Van Paepegem, A.M. Habraken, J. Degrieck, R.J. Alves de Sousa, R.A.F. Valente, Optimal low-order fully integrated solid-shell elements, Comput. Methods Appl. Mech. Eng. 51 (3) (2013) 309–326.

[32] A. Hajlaoui, E. Triki, A. Frikha, M. Wali, F. Dammak, Nonlinear dynamics analysis of FGM shell structures with a higher order shear strain enhanced solid-shell element, Lat. Am. J. Solids Struct. 14 (1) (2017) 72–91.

[33] A. Hajlaoui, A. Jarraya, I. Kallel-Kammoun, F. Dammak, Buckling analysis of a laminated composite plate with delaminations using the enhanced assumed strain solid shell element, J. Mech. Sci. Technol. 26 (10) (2012) 3213–3221.

[34] D. Marinković, H. Köppe, U. Gabbert, Accurate modeling of the electric field within piezoelectric layers for active composite structures, J. Intell. Mater. Syst. Struct. 18 (5) (2007) 503–513.

[35] D. Marinković, H. Köppe, U. Gabbert, Aspects of modeling piezoelectric active thin-walled structures, J. Intell. Mater. Syst. Struct. 20 (15) (2009) 1835–1844.

[36] V. Balamurugan, S. Narayanan, A piezolaminated composite degenerated shell finite element for active control of structures with distributed piezosensors and actuators, Smart Mater. Struct. 17 (3) (2008) 035031.

[37] D. Marinković, M. Zehn, Finite element formulation for active composite laminates, Am. J. Eng. Appl. Sci. 8 (3) (2015) 328.

[38] R. Lammering, S. Mesecke-Rischmann, Multi-field variational formulations and related finite elements for piezoelectric shells, Smart Mater. Struct. 12 (6) (2003) 904.

[39] D. Marinković, H. Köppe, U. Gabbert, Numerically efficient finite element formulation for modeling active composite laminates, Mech. Adv. Mat. Struct. 13 (5) (2006) 379–392.

[40] T. Nestorović, D. Marinković, G. Chandrashekar, Z. Marinković, M. Trajkov, Implementation of a user defined piezoelectric shell element for analysis of active structures, Finite Elem. Anal. Des. 52 (2012) 11–22.

[41] T. Nestorović, D. Marinković, S. Shabadi, M. Trajkov, User defined finite element for modeling and analysis of active piezoelectric shell structures, Meccanica 49 (8) (2014) 1763–1774.

[42] A. Frikha, S. Zghal, F. Dammak, Finite rotation three and four nodes shell elements for functionally graded carbon nanotubes-reinforced thin composite shells analysis, Comput. Methods Appl. Mech. Eng. 329 (2018) 289–311.

[43] G. Bao, L. Wang, Multiple cracking in functionally graded ceramic/metal coatings, Int. J. Solids Struct. 32 (1995) 2853–2871.

[44] Y.S. Touloukian, R.K. Kirby, E.R. Taylor, T.Y.R. Lee, Thermophysical Properties of Matter, Vol. 13. Thermal Expansion-Nonmetallic Solids, TPRC Data Series, Thermophysical and Electronic Properties Information Analysis Center, Lafayette, LA, USA, 1977.
[45] X.Q. He, T.Y. Ng, S. Sivashanker, K.M. Liew, Active control of FGM plates with integrated piezoelectric sensors and actuators, Int. J. Solids Struct. 38 (9) (2001) 1641–1655.
[46] E.F. Crawley, K.B. Lazarus, Induced strain actuation of isotropic and anisotropic plates, AIAA J. 29 (6) (1991) 944–951.